

www.acsami.org Research Article

Two-/Three-Dimensional Perovskite Bilayer Thin Films Post-Treated with Solvent Vapor for High-Performance Perovskite Photovoltaics

Rui Chen, Lening Shen, Luyao Zheng, Tao Zhu, Yanghe Liu, Lei Liu, Jie Zheng, and Xiong Gong*



Cite This: ACS Appl. Mater. Interfaces 2021, 13, 49104–49113



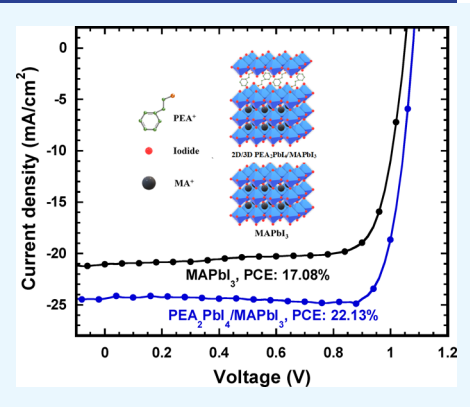
ACCESS

Metrics & More

Article Recommendations

Supporting Information

ABSTRACT: Perovskite photovoltaics (PPVs) using three-dimensional (3D) perovskites incorporated with two-dimensional (2D) perovskites have drawn great concentration in both academic and industrial sectors. Here, we report high performance of PPVs based on the 2D/3D perovskite bilayer thin film post-annealed with solvent vapor. The 2D/3D perovskite bilayer thin film post-annealed with solvent vapor possesses enlarged crystal size and crystallinity and blue-shifted photoluminescence compared to a 3D MAPbI₃ thin film. Moreover, compared to the PPVs based on a 3D perovskite thin film, enlarged built-in potential, suppressed charge carrier recombination, boosted charge transport, and reduced charge carrier extraction time are observed from the PPVs based on the 2D/3D perovskite bilayer thin film post-annealed with solvent vapor. As a result, perovskite solar cells exhibit a power conversion efficiency of 22.13% and dramatically enhanced stability, and perovskite photodetectors show a photoresponsivity of 1.38 AW⁻¹, detectivity of 6.52 \times 10¹⁴ cm Hz^{1/2} W⁻¹, and linear dynamic range of over 167 dB at room temperature. These



results demonstrate that we develop a simple method to approach high-performance PPVs by the 2D/3D perovskite bilayer thin film.

KEYWORDS: perovskite photovoltaics, 2D/3D perovskite bilayer thin film, power conversion efficiency, photodetectivity, stability

1. INTRODUCTION

Three-dimensional (3D) hybrid inorganic—organic perovskites have been mightily studied for approaching high-performance perovskite photovoltaics (PPVs) including perovskite solar cells (PSCs) and perovskite photodetectors (PPDs). ^{1–8} Efficient PSCs and ultrasensitive PPDs by 3D perovskites have been demonstrated. ^{1–8} However, 3D perovskites were intrinsically sensitive to moisture and oxygen, which retarded the long-term stability of PPVs. ^{9–11} Through partial substitution of hydrophilic ammonium with organic hydrophobic groups to create two-dimensional (2D) perovskites over 3D perovskites, stable PPVs have been reported. ^{3,12–20} The 2D/3D perovskite bilayer thin films, utilizing both optoelectronic properties of 3D perovskites and waterproof functionalities of 2D perovskites, were a facile way to approach high-performance PPVs. ^{13,21–23}

In the past years, many attempts have been dedicated to developing high-performance PPVs using 2D/3D perovskite bilayer thin films. 3,12-20 Smith et al. reported stable 2D perovskites, where methylammonium (MA⁺) was partially substituted by hydrophobic phenethylammonium (PEA⁺). Tail et al. reported over 12% power conversion efficiency (PCE) from the PSCs by the butylammonium-based perovskites. Recently, Shi et al. reported stable and efficient (a PCE of 17.3%) PSCs using the quasi-2D (4FPEA)₂(MA)₄Pb₅I₁₆ thin film (where 4FPEA is 4-fluoro-

phenethylammonium). However, large alkyl groups within ammonium cations that are used to create 2D perovskites are typical insulating molecules, which inhibit charge transport, resulting in a lower short-circuit photocurrent ($J_{\rm SC}$) compared to those by 3D perovskite thin films. Arious approaches have been attempted to address the poor charge transport of 2D perovskites. Typically, hydrophobic organic spacers, for example, PEA+ and 4FPEA+, were dissolved into N_i 0, dimethylformamide (dimethyl sulfoxide or their mixtures) to make the 2D/3D perovskite bilayer thin films. Arious Park et al. reported boosted PCEs from the PSCs by the 2D/3D perovskite bilayer thin films treated with alcohol solvents. Loo's group has elucidated the role of Lewis basicity of the processing solvents and reported that the solvent with a high Gutmann donor number ($D_{\rm N}$) could coordinate with Pb²⁺ strongly, which could inhibit iodide coordination, resulting in boosted device performance.

Here, high-performance PPVs (both PSCs and PPDs) based on the PEA₂PbI₄/MAPbI₃ bilayer thin film post-annealed with

Received: August 17, 2021 Accepted: September 25, 2021 Published: October 6, 2021





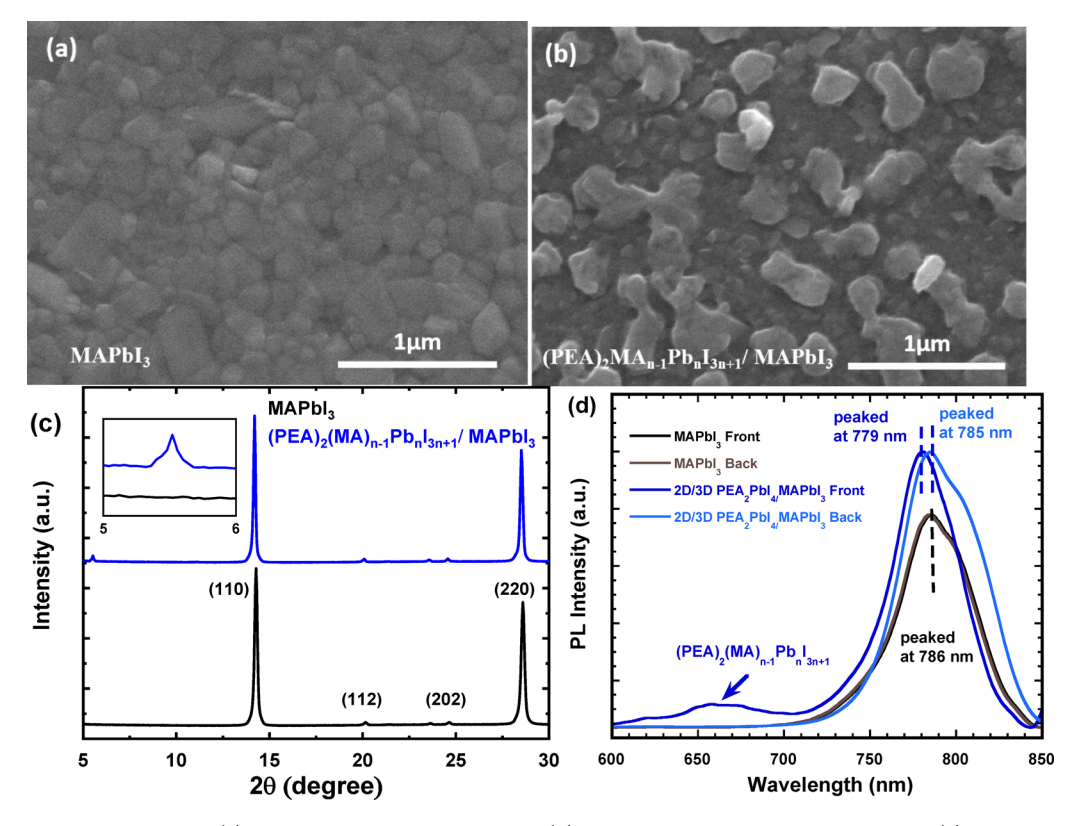


Figure 1. Top view SEM images of (a) the 3D MAPbI₃ thin film and (b) PEA₂PbI₄/MAPbI₃ bilayer thin film; (c) XRD patterns for the 3D MAPbI₃ thin film and PEA₂PbI₄/MAPbI₃ bilayer thin film (the insert is the enlarged diffraction of XRD patterns at a low degree); and (d) photoluminescence (PL) spectra of the 3D MAPbI₃ thin film and PEA₂PbI₄/MAPbI₃ bilayer thin film illuminated from both the front and back sides.

1-butanol vapor are reported. Compared to the 3D MAPbI₃ thin film, the PEA₂PbI₄/MAPbI₃ bilayer thin film postannealed with 1-butanol vapor possesses enlarged crystal size, superior crystallinity, and blue-shifted photoluminescence (PL). Moreover, the PPVs based on the PEA₂PbI₄/MAPbI₃ bilayer thin film post-annealed with 1-butanol vapor exhibit enlarged built-in potential, suppressed charge carrier recombination, boosted charge transport, and reduced charge carrier extraction time, as compared with those based on the 3D MAPbI₃ thin film. Thus, compared to the PPVs based on the 3D MAPbI₃ thin film, the PSCs based on the PEA₂PbI₄/ MAPbI₃ bilayer thin film post-annealed with vapor exhibit a PCE of 22.13% and dramatically enhanced stability. Moreover, at room temperature (RT), the PPDs of the PEA₂PbI₄/ MAPbI₃ bilayer thin film post-annealed with vapor show a significantly reduced dark current density, photoresponsivity of 1.38 AW⁻¹, detectivity of 6.52×10^{14} Jones (1 Jones = 1 cm Hz^{1/2} W⁻¹), and linear dynamic range of over 167 dB.

2. RESULTS AND DISCUSSION

The scanning electron microscopy (SEM) images of the 3D MAPbI $_3$ thin film and the PEA $_2$ PbI $_4$ /MAPbI $_3$ bilayer thin film post-annealed by 1-butanol vapor are shown in Figure 1a,b. 1-Butanol solvent is used to post-treat the PEA $_2$ PbI $_4$ /MAPbI $_3$ bilayer thin film because it possesses a large $D_{\rm N}$, which could inhibit the iodide coordination, resulting in a boosted device performance. Compared to the 3D MAPbI $_3$ thin film, the PEA $_2$ PbI $_4$ /MAPbI $_3$ bilayer thin film post-annealed with 1-butanol vapor possesses a large amount of discretely distributed secondary 2D PEA $_2$ PbI $_4$ crystals over the 3D MAPbI $_3$ thin film. The 3D MAPbI $_3$ thin film possesses a crystal

size of ~100 nm, whereas the PEA₂PbI₄/MAPbI₃ bilayer thin film possesses a crystal size of ~400 nm, thus boosted charge transport; consequently, the PPVs based on the PEA₂PbI₄/MAPbI₃ bilayer thin film is expected to exhibit enlarged enhanced $J_{\rm SC}$.

Figure 1c presents the X-ray diffraction (XRD) patterns of the 3D MAPbI $_3$ thin film and PEA $_2$ PbI $_4$ /MAPbI $_3$ bilayer thin film. Both thin films possess strong peaks at 2θ of 14.3, 20.2, 24.7, and 28.6°, which are ascribed to the (110), (112), (202), and (220) planes, respectively. $^{32-34}$ The full width at half maximum (FWHM) value at the (110) plane observed from the 3D MAPbI $_3$ thin film is 0.17°, whereas the FWHM value at the (110) plane observed from the PEA $_2$ PbI $_4$ /MAPbI $_3$ bilayer thin film is 0.11°. These low FWHM values indicate that both thin films possess large crystallinity, which is ascribed to the one-step self-assembled method used for the preparation of the 3D MAPbI $_3$ thin film. A weak peak at 2θ of 5.5° (the insert of Figure 1c) observed from the PEA $_2$ PbI $_4$ /MAPbI $_3$ bilayer thin films indicates that the 2D PEA $_2$ PbI $_4$ is created above the 3D MAPbI $_3$ thin film. 4

The PL spectra of the 3D MAPbI₃ thin film and PEA₂PbI₄/MAPbI₃ bilayer thin film are displayed in Figure 1d. Two different thin films possess a similar absorption spectrum, but the PEA₂PbI₄/MAPbI₃ bilayer thin film exhibits a slightly blue-shifted PL spectrum, which originated from the existence of a high *n*-value 2D perovskite component (Figure S1, SI).³ Furthermore, the 3D MAPbI₃ thin film exhibits an identical PL spectrum illuminated either from the front side or the backside. While the PL spectrum of the PEA₂PbI₄/MAPbI₃ bilayer thin film illuminated from the front side is different from that illuminated from the backside. Such a difference in PL spectra

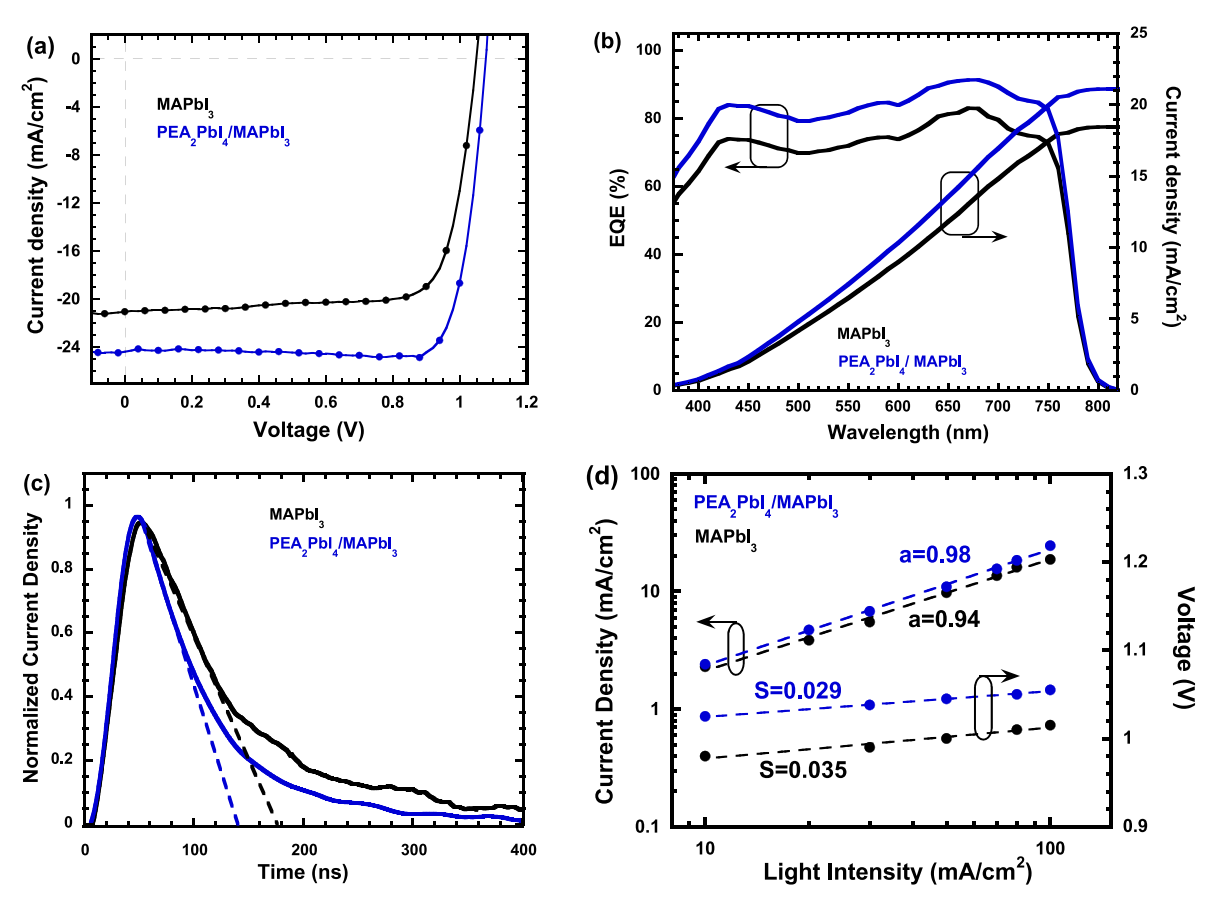


Figure 2. (a) J-V characteristics of PSCs, (b) EQE spectra and integrated J_{SC} of PSCs, (c) normalized transient photocurrent curves of PSCs, and (d) light intensity dependence of J_{SC} and V_{OC} for PSCs, where the PSCs are fabricated using either the 3D MAPbI₃ thin film or PEA₂PbI₄/MAPbI₃ bilayer thin film.

further confirms that the 2D PEA_2PbI_4 thin layer is formed above the 3D MAPbI₃ thin film.^{3,4,12-17} In addition, a broad peak located at ~660 nm within the $PEA_2PbI_4/MAPbI_3$ bilayer thin film further demonstrates the high n value of the 2D perovskite structure.³ These results indicate the disparate phase distribution for the $PEA_2PbI_4/MAPbI_3$ bilayer thin film.

The photovoltaic properties of the PEA₂PbI₄/MAPbI₃ bilayer thin film are studied through the investigation of the PPVs with a device architecture of ITO/PTAA/perovskite active layer/C₆₀/BCP/Al, where ITO is indium tin oxides and acts as the anode, PTAA is poly[bis(4-phenyl)(2,4,6trimethylphenyl)amine] and serves as the hole extraction layer, the perovskite active layer is either the PEA2PbI4/ $MAPbI_3$ bilayer thin film or $3D\ MAPbI_3$ thin film, C_{60} is fullerene and acts as the electron extraction layer, BCP is bathocuproine and is used as the hole-blocking layer, and Al is aluminum and acts as the cathode. The current density versus voltage (J-V) characteristics of the PSCs by the 3D MAPbI₃ thin film and PSCs by the PEA₂PbI₄/MAPbI₃ bilayer thin films are shown in Figure 2a (and Figure S2). Table S1 summarizes the device performance parameters of PSCs. At a scan rate of 0.60 V s⁻¹, the PSCs based on the 3D MAPbI₃ thin film exhibit a $V_{\rm OC}$ of 1.04 V, $J_{\rm SC}$ of 21.05 mA cm⁻², and fill factor (FF) of 78%, with a PCE of 17.08%. These device performance parameters are consistent with the reported values from the PSCs with a similar device structure. 35-38 The best device performance of the PSCs based on the PEA₂PbI₄/MAPbI₃ bilayer thin film exhibit a $V_{\rm OC}$ of 1.08 V, $J_{\rm SC}$ of 24.39 mA cm⁻², and FF of 84%, with a PCE of 22.13%, which is an

approximately 30% enhancement compared to that based on the 3D $MAPbI_3$ thin film.

The external quantum efficiency (EQE) spectra and integrated J_{SC} of PSCs are shown in Figure 2b. Compared to the PSCs based on the 3D MAPbI₃ thin film, the EQE spectrum of the PSCs based on the PEA₂PbI₄/MAPbI₃ bilayer thin film exhibits a distinct enhancement from 375 to 760 nm. By integration of the EQE spectrum, the integrated J_{SC} values are estimated. An integrated J_{SC} of 19.94 mA cm⁻² is for the PSCs based on the 3D MAPbI₃ thin film, and an integrated J_{SC} of 22.53 mA cm⁻² is for the PSCs based on the PEA₂PbI₄/MAPbI₃ bilayer thin film. Both the integrated and extracted (the J-V characteristics Figure 2a) J_{SC} values are nearly the same.

The transient photocurrent (TPC) measurement is used to estimate the charge carrier extraction time of PSCs for investigating the underlying physics of enhanced J_{SC} from the PSCs based on the PEA₂PbI₄/MAPbI₃ bilayer thin film. ^{34–42} Figure 2c displays the normalized TPC curves of PSCs. The charge carrier extraction time for the PSCs based on the PEA₂PbI₄/MAPbI₃ bilayer thin film is estimated to be 141 ns, which is shorter than that (177 ns) for the PSCs based on the 3D MAPbI₃ thin film, revealing that the charge carrier extraction is efficient and the charge carrier recombination is suppressed within the PSCs. Thus, the PSCs based on the PEA₂PbI₄/MAPbI₃ bilayer thin film exhibit enhanced J_{SC} . Moreover, the extracted charge carrier densities of the PSCs based the 3D MAPbI₃ thin film are smaller than those based on the PEA₂PbI₄/MAPbI₃ bilayer thin film (Figure S3), which

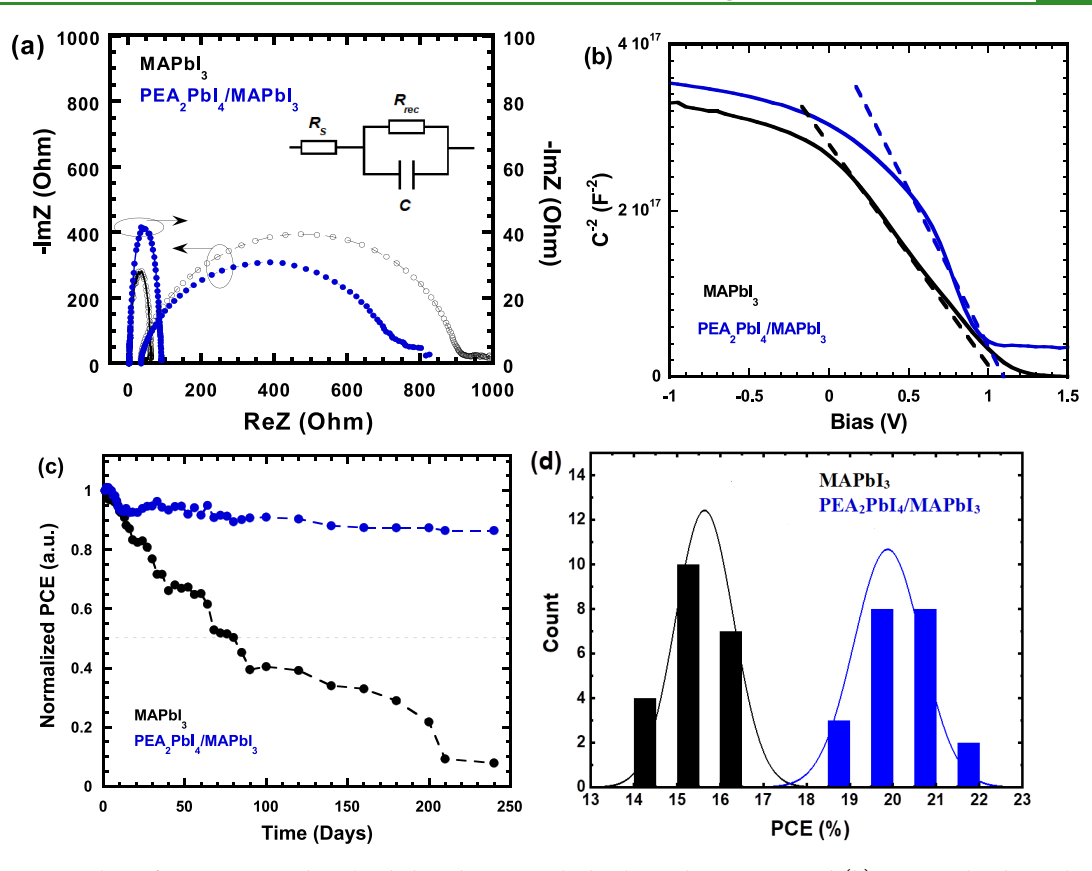


Figure 3. (a) Nyquist plots of PSCs measured in the dark and at an applied voltage close to $V_{\rm OC}$ and (b) Mott–Schottky analysis for the trap density and built-in potential of PSCs. (c) Normalized shelf stability and (d) histograms of PCEs of PSCs, where the PSCs are fabricated using either the 3D MAPbI₃ thin film or PEA₂PbI₄/MAPbI₃ bilayer thin film.

further indicates that the PSCs based on the $PEA_2PbI_4/MAPbI_3$ bilayer thin film exhibit boosted J_{SC} .

Figure 2d presents the light intensity dependence of J_{SC} and $V_{\rm OC}$ of PSCs. Both the $J_{\rm SC}$ and $V_{\rm OC}$ of PSCs depend on light intensity (*I*). According to the power law of $J_{sc} \propto I^{\alpha}$ (where α is the scaling exponent), 43 an α of 0.94 is observed from the PSCs based on the 3D MAPbI₃ thin film, whereas an α of 0.98 is observed from the PSCs based on the PEA2PbI4/MAPbI3 bilayer thin film. As the α value is close to 1, the nongerminate charge carrier recombination is suppressed. 43 Thus, the PSCs based on the PEA₂PbI₄/MAPbI₃ bilayer thin film exhibit enhanced Isc and consequently boosted PCEs. Moreover, based on $V_{OC} \propto S \ln (I)$ (where S is the slope), ⁴³ an S of 0.035 is observed from the PSCs based on the 3D MAPbI₃ thin film, whereas an S of 0.029 is observed from the PSCs based on the PEA₂PbI₄/MAPbI₃ bilayer thin film. As S approaches $\frac{kT}{a}$ (0.026) (where k is the Boltzmann constant, T is the absolute temperature, and q is the elementary charge), the trap-assistant charge carrier recombination within the PSCs is suppressed. Thus, a high α and small S observed from the PSCs based on the PEA₂PbI₄/MAPbI₃ bilayer thin film indicate that the charge carrier recombination is suppressed, resulting in enhanced J_{sc} and consequently boosted PCE.

Figure 3a displays the Nyquist plots of PSCs measured in the dark and under an applied voltage at $\sim V_{\rm OC}$. As the IS is conducted in the dark and under an applied voltage at $V_{\rm OC}$, the charge carrier recombination resistance ($R_{\rm rec}$) is minimized and the charge transfer resistance ($R_{\rm CT}$) is dominated in PSCs. ^{43,44} Thus, a simplified equivalent circuit is presented in the inset of Figure 3a, where $R_{\rm s}$, the sheet resistance of the conductive

electrode, is the same, which is based on the identical device structure of PSCs under the investigation. 43,44 The R_{CT} is affected by the perovskite photoactive layers. The semicircle presented in Figure 3a indicates that not only the RC circuit model is accurate (insert of Figure 3a) but also the transport pathways are homogeneous without discernible multiple interfacial boundaries. Hence, R_{CT} values for the PSCs based on the 3D MAPbI₃ thin film and the PSCs based on the PEA₂PbI₄/MAPbI₃ bilayer thin film are 1002 and 803 Ω , respectively. A smaller R_{CT} observed from the PSCs by the PEA₂PbI₄/MAPbI₃ bilayer thin film is ascribed to superior surface coverage, optimal film morphology, and suppressed defect-induced traps. Thus, reduced R_{CT} indicates that charge transport is boosted, resulting in enhanced J_{SC} and PCEs for the PSCs based on the PEA₂PbI₄/MAPbI₃ bilayer thin film.

The impedance spectra (IS) (Nyquist plots) of PSCs measured under white illumination with a light intensity of 100 mW cm $^{-2}$ and at an applied voltage of $\sim\!\!V_{\rm OC}$ are shown in Figure 3a. Under these conditions, the charge carrier recombination resistance ($R_{\rm rec}$) is dominated within PSCs. $R_{\rm rec}$ values of 60 and 90 Ω are observed from the PSCs based on the 3D MAPbI $_3$ thin film and the PSCs based on the PEA $_2$ PbI $_4$ /MAPbI $_3$ bilayer thin film, respectively. A larger $R_{\rm rec}$ indicates that the PSCs possess a suppressed charge carrier recombination. Therefore, boosted $J_{\rm SC}$ is observed from the PSCs based on the PEA $_2$ PbI $_4$ /MAPbI $_3$ bilayer thin film.

The charge carrier mobilities of the 3D MAPbI $_3$ thin film and PEA $_2$ PbI $_4$ /MAPbI $_3$ bilayer thin film are further investigated through the space charge limited current method based on the Mott–Gurney law, 46,47 and the results are shown in

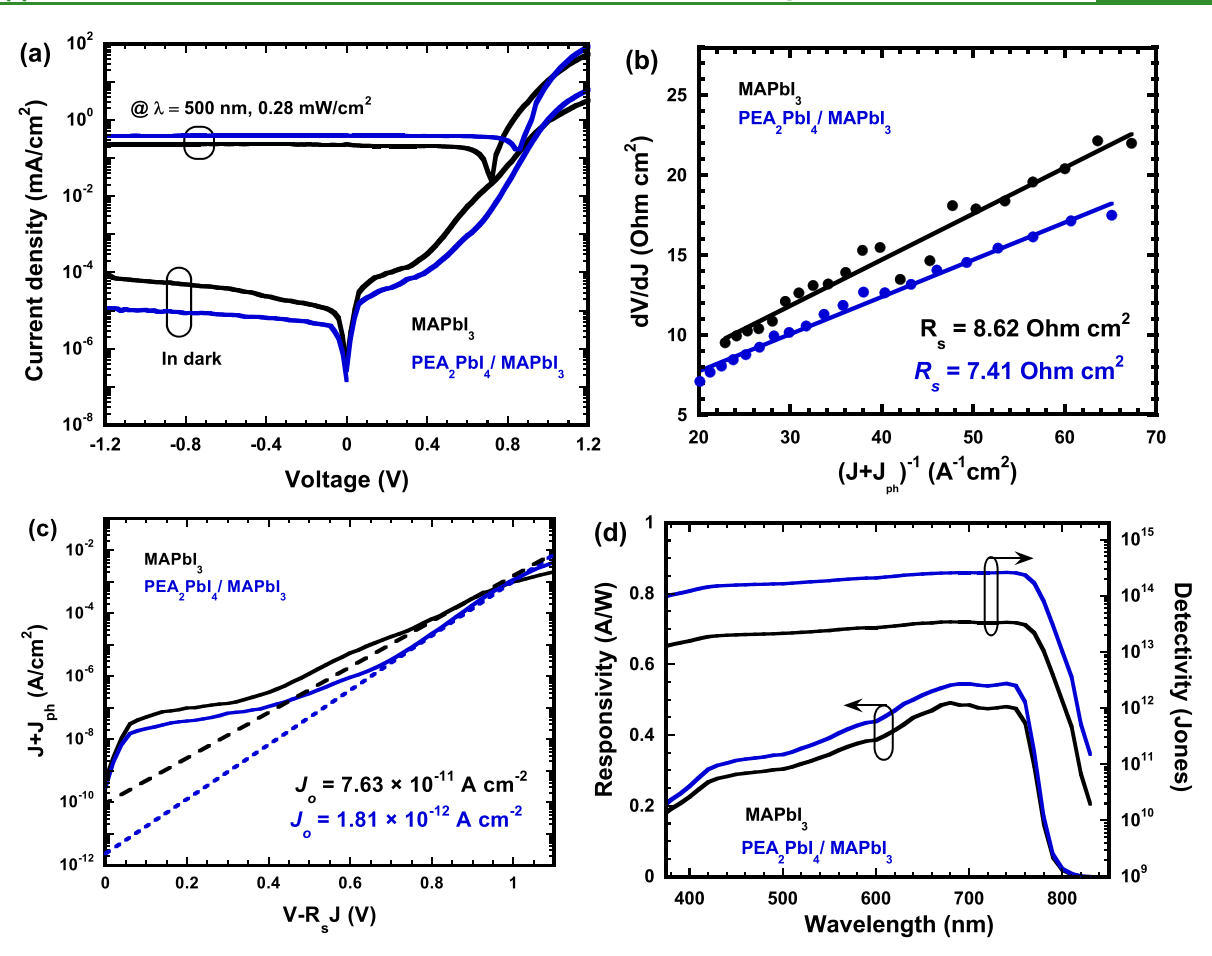


Figure 4. (a) J-V characteristics of PPDs measured both in the dark and under monochromatic illumination at a wavelength of 500 with a light intensity of 0.28 mW/cm² at room temperature for PPDs, (b) plot of $\frac{V}{dJ}$ versus $(J_{\rm ph} + J)^{-1}$ and linear fitting of PPDs, (c) plot of $(J_{\rm ph} + J)^{-1}$ versus $(V - R_S J)$ and the linear fitting of PPDs, (d) responsivity and detectivity versus wavelength for PPDs measured at a bias of -0.10 V, where the PPDs are fabricated using either the 3D MAPbI₃ thin film or PEA₂PbI₄/MAPbI₃ bilayer thin film.

Figures S4 and S5 (Scheme S3). A hole mobility of 6.62×10^{-3} cm² V⁻¹S⁻¹ and electron mobility of 5.94×10^{-3} cm² V⁻¹S⁻¹ are observed from the 3D MAPbI₃ thin film. A hole mobility of 7.91×10^{-3} cm² V⁻¹S⁻¹ and electron mobility of 7.16×10^{-3} cm² V⁻¹S⁻¹ are observed from the PEA₂PbI₄/MAPbI₃ bilayer thin film. Thus, the PEA₂PbI₄/MAPbI₃ bilayer thin film exhibits both enhanced hole and electron mobilities, indicating that the charge transport is boosted. As a result, enhanced $J_{\rm SC}$ and enlarged FF are observed from the PSCs based on the PEA₂PbI₄/MAPbI₃ bilayer thin film.

To understand an enlarged $V_{\rm OC}$ from the PSCs based on the PEA₂PbI₄/MAPbI₃ bilayer thin film, the J-V characteristics of PSCs are measured in the dark and the results are shown in

Figure 4a.
$$V_{\rm oc}$$
 is described as $V_{\rm oc} = \frac{nkT}{q} \ln \left(\frac{J_{\rm SC}}{J_{\rm d}}\right)$, 40–42 where n is the ideality factor (approaches 2) for PSCs, 46 k is the Boltzmann constant, T is the absolute temperature, q is the electron charge, and $J_{\rm d}$ is the reverse dark current density. It is concluded that the suppressed dark current density is a response for the enlarged $V_{\rm OC}$. It is found that PSCs based on the PEA₂PbI₄/MAPbI₃ bilayer thin film exhibit lower dark current densities than those based on the 3D MAPbI₃ thin film. Thus, the PSCs based on the PEA₂PbI₄/MAPbI₃ bilayer thin film possesses larger $V_{\rm OC}$ with respect to that based on the 3D MAPbI₃ thin film.

Both the built-in potential $(V_{\rm bi})$ and interfacial charge density (N) of PSCs are estimated based on the capacitance versus voltage (C-V) characteristics of PSCs. According to the Mott–Schottky law of $C^{-2} = \frac{2(V_{\rm bi}-V)}{qe\varepsilon_0A^2n_c}$ (where V is the applied bias of it the algorithm above S is the dislocation constant of

bias, q is the elementary charge, ε is the dielectric constant of perovskites, ε_0 is the vacuum permittivity, n_c is the charge carrier density, and A is the active area.), the $V_{\rm bi}$ is the intercept on the bias of the linear fitting line and the N is obtained from the slope of the linear fitting. 35,48 The $C^{-2}-V$ plot of PSCs is shown in Figure 3b. The PSCs based on the PEA₂PbI₄/ MAPbI₃ bilayer thin film exhibit a $V_{\rm bi}$ of 1.10 V, which is larger than that (1.04 V) based on the 3D MAPbI₃ thin film. These results indicate that the PSCs based on the PEA₂PbI₄/MAPbI₃ bilayer thin film exhibit larger $V_{\rm OC}$ compared to that based on the 3D MAPbI₃ thin film. Moreover, the slope of the $C^{-2}-V$ line for the PSCs based on the 3D MAPbI3 thin film is estimated to be -2.69×10^{17} , which is higher than $-3.95 \times$ 10¹⁷ based on the PEA₂PbI₄/MAPbI₃ bilayer thin film. Such a larger absolute slope value observed from the PSCs based on the PEA₂PbI₄/MAPbI₃ bilayer thin film indicates that PSCs possess a smaller interfacial charge density. 49,50 As a result, the surface charge carrier recombination is suppressed, which results in enhanced J_{SC} for the PSCs based on the PEA₂PbI₄/ MAPbI₃ bilayer thin film.

The shelf stability of unencapsulated PSCs is tested in ambient conditions. As indicated in Figure 3c, the PSCs based on the 3D MAPbI₃ thin film drop their PCEs to 45% after 85 days. Under the same condition, the PCE values of the PSCs based on the PEA₂PbI₄/MAPbI₃ bilayer thin film maintain 86.5% of their initial PCEs for 240 days. Both PSCs show degradation in J_{SC} after 240 days (Figure S6), but the PSCs based on the 3D MAPbI₃ thin film decreased from 1.04 to 0.98 V after 240 days, whereas the PSCs based on the PEA₂PbI₄/ MAPbI $_3$ bilayer thin film shows negligible degradation in $V_{\rm OC}$ after 240 days. Furthermore, the PSCs based on the 3D MAPbI₃ thin film present a significantly declined FF, whereas the PSCs based on the PEA2PbI4/MAPbI3 bilayer thin film maintain nearly the same level of the FF for 240 days. Thus, compared to PSCs based on the 3D MAPbI3 thin film, the PSCs based on the PEA₂PbI₄/MAPbI₃ bilayer thin film possess dramatically enhanced stability, which reveals that the 2D perovskite layer plays a very important role in manufacturing long-term stable PSCs and preventing the 3D perovskite layer underneath from moisture.

The reproducibility of PSCs is further investigated. The statistical histograms of PCEs with Gaussian fitting for PSCs from over 20 devices are shown in Figure 3d and Figure S7. The PSCs based on either the 3D MAPbI₃ thin film or 2D/3D PEA₂PbI₄/MAPbI₃ bilayer thin film display a compact distribution of device performance parameters, which indicates good reproducibility of PSCs. With respect to that based on the 3D MAPbI₃ thin film, the PSCs based on the PEA₂PbI₄/ MAPbI₃ bilayer thin film present a narrower distribution, indicating that the PSCs possess superior reproducibility. Such high reproducibility is ascribed to the uniform and homogeneous film morphology of the PEA2PbI4/MAPbI3 bilayer thin film.51,52

PPDs are also investigated. The J-V characteristics of PPDs measured both in the dark and under monochromatic illumination at a λ of 500 nm with a light intensity of 0.28 mW/cm² at room temperature (RT) are shown in Figure 4a. At a bias of -0.10 V, the dark current density (I_d) observed from the PPDs based on the PEA2PbI4/MAPbI3 bilayer thin film is 4.20×10^{-9} A cm⁻², which is almost three times lower than that $(1.14 \times 10^{-8} \text{ A cm}^{-2})$ based on the 3D MAPbI₃ thin film. The decreased I_d indicates that the leakage current from the PPDs based on the PEA2PbI4/MAPbI3 bilayer thin film is suppressed. The low dark current density is attributed to the reduced defects within the PEA₂PbI₄/MAPbI₃ bilayer thin film (Figure 3b) and indicates that the PPDs based on the PEA₂PbI₄/MAPbI₃ bilayer thin film possess boosted projected detectivity (D*).52 Moreover, under monochromatic illumination at $\lambda = 500$ nm with a light intensity of 0.28 mW/cm² at RT, the photocurrent density (J_{ph}) of the PPDs based on the $PEA_2PbI_4/MAPbI_3$ bilayer thin film is 3.85×10^{-4} A cm⁻², which is higher than that $(2.26 \times 10^{-4} \text{ A cm}^{-2})$ based on the 3D MAPbI₃ thin film. The responsivity (R) is described as $R = \frac{J_{\rm ph}}{L_{\rm light}}$ (where $L_{\rm light}$ is the incident light intensity). 52 An R of 0.81 A W⁻¹ is observed from the PPDs based on the 3D $MAPbI_3$ thin film, whereas an R of 1.38 A W^{-1} is observed from the PPDs based on the PEA2PbI4/MAPbI3 bilayer thin

Based on the J-V curves of PPDs measured in the dark, the *J*–*V* curves are extracted to estimate the saturated dark current densities $(J_0)^{.7,52}$ J_0 , a key factor determining the D^* of photodetectors (PDs), is related to the charge carrier

recombination and band-to-band thermal emission in PDs. 53-55 Due to the complicated and expensive setup, J_0 is relatively difficult to be measured, \overline{I}_0 can be estimated since J_0 is described as $J = J_0 \left[\exp \left(\frac{q(V - JR_s)}{nk_b T} \right) - 1 \right] - J_{\rm ph}$ (where *J* is the total current density, *q* is the elementary electron charge, V is the applied voltage, R_s is the series resistance, n is the idea factor, k_b is the Boltzmann constant, and T is the absolute temperature). Figure 4b displays the plot of $\frac{V}{dI}$ versus $(J_{\rm ph} + J)^{-1}$ and linear fitting of PPDs. The $R_{\rm s}$ value is extracted from the linear fitting intercept (see detailed calculation in the SI). R_s values of 8.62 and 7.41 Ω are calculated for the PPDs based on the 3D MAPbI3 thin film and $PEA_2PbI_4/MAPbI_3$ bilayer thin film, respectively. A smaller R_s observed from the PPDs based on the PEA₂PbI₄/MAPbI₃ bilayer thin film indicates that PPDs possess a higher $J_{\rm ph}$ compared to that based on the 3D MAPbI₃ thin film. Figure 4c exhibits the $ln(J + J_{ph})$ versus $(V - R_S J)$ characteristics and linear fitting intercepts of PPDs. A J_0 of 1.18×10^{-12} A cm⁻² is estimated for the PPDs based on the PEA₂PbI₄/MAPbI₃ bilayer thin film, whereas a J_0 of 7.63×10^{-11} Å cm⁻² is estimated for the PPDs based on the 3D MAPbI3 thin film. Thus, compared to the PPDs based on the 3D MAPbI₃ thin film, a higher $J_{\rm ph}$ and a lower J_0 were observed from the PPDs based on the PEA₂PbI₄/MAPbI₃ bilayer thin film further,

The D^* is described as $D^* = \frac{R}{\sqrt{2qJ_d}} = \frac{J_{\rm ph}}{\sqrt{2qJ_d}}, ^{56}$ (where $L_{\rm light}$ is the light intensity, J_d is the dark current density, and q is the elementary electron charge.). At a λ of 500 nm with a light intensity of 0.28 mW cm $^{-2}$ and under an external bias of -0.10V, a D^* of 5.66 \times 10¹³ Jones (1 Jones = 1 cm Hz^{1/2} W⁻¹) is observed from the PPDs based on the 3D MAPbI3 thin film, whereas a D^* of 6.52×10^{14} Jones is observed from the PPDs based on the PEA₂PbI₄/MAPbI₃ bilayer thin film. Note that the above D^* is solely calculated based on the measured dark current, probably resulting in a higher D^* with respect to the real detectivity, since both the thermal (Johnson) noise and flicker noise 1/f (where f is the frequency) are neglected. 56-58Nevertheless, D* is acceptable because the noise current is in the same magnitude as the shot noise originating from the dark current and is generally frequency-independent for PDs with a vertical photodiode device structure. 57,39,60

which indicates that PPDs exhibit both higher R and D^* .

Based on the EQE spectra, both R and D^* over spectral response are calculated according to $R = \text{EQE} \times \frac{q}{h\nu} = \text{EQE} \times \frac{\lambda}{1240}$ and $D^* = \frac{R}{\sqrt{2qJ_d}}$. Figure 4d

presents R and D^* versus wavelength from 375 to 830 nm. At RT, the PPDs based on the PEA₂PbI₄/MAPbI₃ bilayer thin film exhibit significantly higher R and D^* compared to those from the PPDs based on the 3D MAPbI3 thin film. For example, the PPDs based on the PEA₂PbI₄/MAPbI₃ bilayer thin film exhibit over 10^{14} Jones D^* , which is 10 times higher than those based on the 3D MAPbI₃ thin film. Moreover, this value is higher than that of Si-based PDs in the spectral range from 375 to 700 nm.7 Such high detectivity at RT is synergistically derived from high $J_{\rm ph}$ and very low $J_{\rm d}$. 54,55,61 The linear dynamic range (LDR) described as the

photocurrent correlated with a linear response along with the incident light intensity is further investigated. The LDR is described by LDR = 20 log (J_{ph}/J_d) , where J_{ph} is the photocurrent measured at a light intensity of 1 mW/cm² and

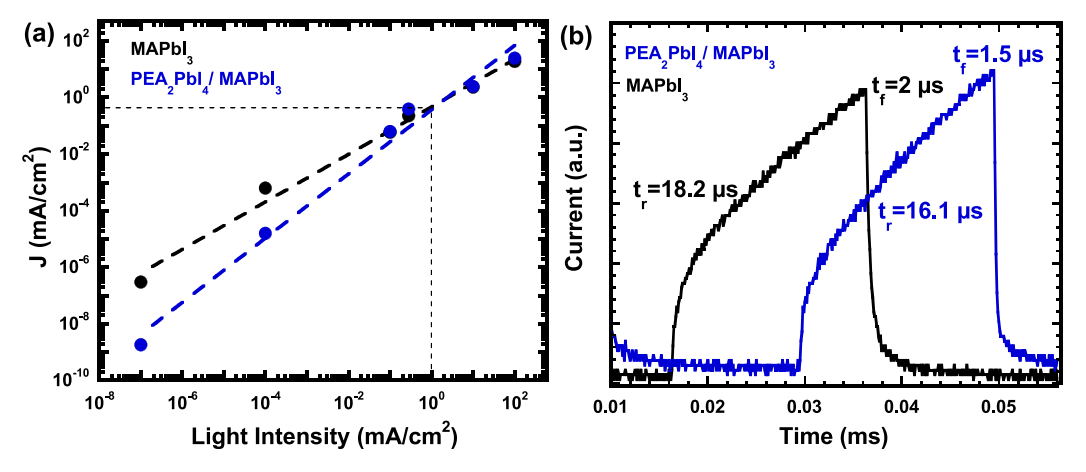


Figure 5. (a) Linear dynamic range (LDR) of PPDs, (b) temporal photocurrent response of PPDs measured with an optical chopper (a frequency of 2 kHz) controlled at a wavelength of 532 nm laser pulse, where the PPDs are fabricated using either the 3D MAPbI₃ thin film or PEA₂PbI₄/MAPbI₃ bilayer thin film.

 $J_{\rm d}$ is the dark current. Figure 5a displays the $J_{\rm ph}$ versus the light intensities for PPDs at RT. An LDR of ~122 dB observed from the PPDs based on the 3D MAPbI₃ thin film is smaller than that (~167 dB) observed from the PPDs based on the PEA₂PbI₄/MAPbI₃ bilayer thin film. Both are higher than those from Si-based PDs (120 dB, at 77 K) and InGaAs-based PDs (66 dB, at 4.2 K). S4

The temporal photocurrent response time of PPDs is another important device parameter of PDs. 62 The response time of PDs is significantly related to the charge transport and collection. The rise and fall times are defined as the time interval required for the photoresponse to rise/decay from 10/ 90 to 90/10% of its peak photocurrent value, respectively.⁶² The temporal photocurrent responses of PPDs measured with an optical chopper (a frequency of 2 k Hz) controlled by a 532 nm λ laser pulse are shown in Figure 5b. A rise time of 18.2 μ s and a fall time of 2.0 μ s are observed from the PPDs based on the 3D MAPbI₃ thin film, whereas a rise time of 16.1 μ s and a fall time of 1.5 μ s are observed from the PPDs based on the PEA₂PbI₄/MAPbI₃ bilayer thin film. The faster response times observed from the PPDs based on the PEA2PbI4/MAPbI3 bilayer thin film are attributed to the enhanced charge carrier transport and suppressed defects of the PEA₂PbI₄/MAPbI₃ bilayer thin film.

3. CONCLUSIONS

In summary, we reported the formation of the PEA₂PbI₄/ MAPbI₃ bilayer thin films post-annealed with 1-butanol vapor. Systematical studies demonstrated that the PEA₂PbI₄/MAPbI₃ bilayer thin films post-annealed with 1-butanol vapor possessed superior crystallinity and boosted charge transport. Moreover, compared to perovskite photovoltaics (PPVs) based on the 3D MAPbI₃ thin film, PPVs based on the PEA₂PbI₄/MAPbI₃ bilayer thin film exhibited increased built-in potential, suppressed charge carrier recombination, and boosted charge transport. As a result, we observed high performance, in terms of power conversion efficiency, photodetectivity, and stability, from PPVs based on the PEA₂PbI₄/MAPbI₃ bilayer thin films post-treated with 1-butanol vapor annealing. For example, over 22% power conversion efficiency and dramatically enhanced stability were observed from perovskite solar cells. Moreover, over 1014 Jones detectivity and a large linear dynamic range of 167 dB were observed from perovskite photodetectors. These

results demonstrated that we have developed a simple method to approach high-performance PPVs.

4. EXPERIMENTAL SECTION

4.1. Materials. Methylammonium iodide (MAI, 99.9%) was purchased from GreatCell Solar. Phenethylammonium iodide (PEAI, 99.9%) was purchased from Sigma-Aldrich. Lead iodide (PbI $_{2}$, 99.9985%, metals basis) was purchased from Alfa Aesar. Poly[bis(4-phenyl)(2,4,6-trimethylphenyl)amine] (PTAA), bathocuproine (BCP, 99.99%), fullerene (C_{60} , 99.5%), bathocuproine, methylamine (MA) (33 wt % in absolute ethanol), anhydrous acetonitrile (ACN, 99.8%), isopropanol (99.5%), 1-butanol (99.8%), γ -butyrolactone (GBL, 99%), and toluene (99.8%) were purchased from Sigma-Aldrich. All chemicals were used as received without any further purification.

4.2. Preparation and Characterization of Perovskite Thin Films. The MAPbI₃ single crystal was grown, and the MAPbI₃ ACN solution was followed from previous reports. ^{29,35} The preparation procedures of the PEA₂PbI₄/MAPbI₃ bilayer thin films are schematically displayed in Scheme S1. A PEAI 1-butanol solution (80 μ L, 1 mg/mL) was dropped on the surface of the 3D MAPbI₃ thin film and kept for 10 s before starting the spin-coating process (6000 RPM for 30 s). The resultant thin films were thermally annealed at 100 °C under 1-butanol vapor for 5 min.

The XRD patterns, ultraviolet–visible (UV–vis) absorption spectra, PL spectra, top-view SEM images, and thicknesses of the perovskite thin films were characterized as described in our previous publications. $^{6,7,35-38}$

4.3. Fabrication and Characterization of Photovoltaic Devices. The procedures of the PPV fabrication and characterization are the same as previously reported. $^{6,7,35-38}$ The device area was measured to be $0.043~\rm cm^2$. A specific wavelength was obtained using a spectrum filter for giving a monochromic light at a wavelength (λ) of 500 nm with a light intensity of 0.28 mW cm⁻². The transient photocurrent (TPC) measurement was described as reported previously. $^{36-38}$ The temporal photocurrent response time of PPDs was performed on a homemade setup using an optical chopper with a wavelength of 532 nm laser pulse at a frequency of 2 kHz. Note that the speed of the optical chopper frequency or duty cycle is in the range of nanoseconds.

ASSOCIATED CONTENT

Supporting Information

The Supporting Information is available free of charge at https://pubs.acs.org/doi/10.1021/acsami.1c15735.

Preparation of perovskite thin films; characterization of perovskite thin films; characterization of perovskite solar

cells;, and characterization of perovskite photodetectors (PDF)

AUTHOR INFORMATION

Corresponding Author

Xiong Gong — School of Polymer Science and Polymer Engineering, The University of Akron, Akron, Ohio 44325, United States; orcid.org/0000-0001-6525-3824; Email: xgong@uakron.edu; Fax: (330) 972-3406

Authors

- Rui Chen School of Polymer Science and Polymer Engineering, The University of Akron, Akron, Ohio 44325, United States
- Lening Shen School of Polymer Science and Polymer Engineering, The University of Akron, Akron, Ohio 44325, United States
- Luyao Zheng School of Polymer Science and Polymer Engineering, The University of Akron, Akron, Ohio 44325, United States
- Tao Zhu School of Polymer Science and Polymer Engineering, The University of Akron, Akron, Ohio 44325, United States
- Yanghe Liu School of Polymer Science and Polymer Engineering, The University of Akron, Akron, Ohio 44325, United States
- Lei Liu School of Polymer Science and Polymer Engineering, The University of Akron, Akron, Ohio 44325, United States
- Jie Zheng Department of Chemical, Biomolecular and Corrosion Engineering, College of Engineering and Polymer Science, The University of Akron, Akron, Ohio 44325, United States; orcid.org/0000-0003-1547-3612

Complete contact information is available at: https://pubs.acs.org/10.1021/acsami.1c15735

Author Contributions

§R.C., L.S., and L.Z. equally contributed to this work
Notes

The authors declare no competing financial interest.

ACKNOWLEDGMENTS

The authors thank the National Science Foundation (EECs 1903303) and Air Force Office of Scientific Research (AFOSR) (through the Organic Materials Chemistry Program, grant number: FA9550-15-1-0292, program manager, Dr. Kenneth Caster) for financial support.

■ REFERENCES

- (1) Cao, D. H.; Stoumpos, C. C.; Farha, O. K.; Hupp, J. T.; Kanatzidis, M. G. 2D Homologous Perovskites as Light-Absorbing Materials for Solar Cell Applications. *J. Am. Chem. Soc.* **2015**, *137*, 7843–7850.
- (2) Chen, X.; Ding, M.; Luo, T.; Ye, T.; Zhao, C.; Zhao, Y.; Zhang, W.; Chang, H. Self-Assembly of 2D/3D Perovskites by Crystal Engineering for Efficient Air-Processed, Air-Stable Inverted Planar Perovskite Solar Cells. ACS Appl. Energy Mater. 2020, 3, 2975–2982.
- (3) Shi, J.; Gao, Y.; Gao, X.; Zhang, Y.; Zhang, J.; Jing, X.; Shao, M. Fluorinated Low-Dimensional Ruddlesden—Popper Perovskite Solar Cells with over 17% Power Conversion Efficiency and Improved Stability. *Adv. Mater.* **2019**, *31*, 1901673.
- (4) Jiang, Q.; Zhao, Y.; Zhang, X.; Yang, X.; Chen, Y.; Chu, Z.; Ye, Q.; Li, X.; Yin, Z.; You, J. Surface Passivation of Perovskite Film for Efficient Solar Cells. *Nat. Photonics* **2019**, *13*, 460–466.

- (5) Luo, D.; Yang, W.; Wang, Z.; Sadhanala, A.; Hu, Q.; Su, R.; Shivanna, R.; Trindade, G. F.; Watts, J. F.; Xu, Z.; Liu, T.; Chen, K.; Ye, F.; Wu, P.; Zhao, L.; Wu, J.; Tu, Y.; Zhang, Y.; Yang, X.; Zhang, W.; Friend, R. H.; Gong, Q.; Snaith, H. J.; Zhu, R. Enhanced Photovoltage for Inverted Planar Heterojunction Perovskite Solar Cells. Science 2018, 360, 1442.
- (6) Xu, W.; Zhu, T.; Yang, Y.; Zheng, L.; Liu, L.; Gong, X. Enhanced Device Performance of Perovskite Photovoltaics by Magnetic Field-Aligned Perovskites-Magnetic Nanoparticles Composite Thin Film. *Adv. Funct. Mater.* **2020**, *30*, 2002808.
- (7) Zheng, L.; Wang, K.; Zhu, T.; Liu, L.; Zheng, J.; Gong, X. Solution-Processed Ultrahigh Detectivity Photodetectors by Hybrid Perovskite Incorporated with Heterovalent Neodymium Cations. *ACS Omega* **2019**, *4*, 15873–15878.
- (8) Zhu, T.; Yang, Y.; Gong, X. Recent Advancements and Challenges for Low-Toxicity Perovskite Materials. *ACS Appl. Mater. Interfaces* **2020**, *12*, 26776–26811.
- (9) Frost, J. M.; Butler, K. T.; Brivio, F.; Hendon, C. H.; van Schilfgaarde, M.; Walsh, A. Atomistic Origins of High-Performance in Hybrid Halide Perovskite Solar Cells. *Nano Lett.* **2014**, *14*, 2584–2590
- (10) Leguy, A. M. A.; Hu, Y.; Campoy-Quiles, M.; Alonso, M. I.; Weber, O. J.; Azarhoosh, P.; van Schilfgaarde, M.; Weller, M. T.; Bein, T.; Nelson, J.; Docampo, P.; Barnes, P. R. F. Reversible Hydration of CH₃NH₃PbI₃ in Films, Single Crystals, and Solar Cells. *Chem. Mater.* **2015**, *27*, 3397–3407.
- (11) Wang, Q.; Chen, B.; Liu, Y.; Deng, Y.; Bai, Y.; Dong, Q.; Huang, J. Scaling Behavior of Moisture-Induced Grain Degradation in Polycrystalline Hybrid Perovskite Thin Films. *Energy Environ. Sci.* **2017**, *10*, 516–522.
- (12) Smith, I. C.; Hoke, E. T.; Solis-Ibarra, D.; McGehee, M. D.; Karunadasa, H. I. A Layered Hybrid Perovskite Solar-Cell Absorber with Enhanced Moisture Stability. *Angew. Chem., Int. Ed.* **2014**, *53*, 11232–11235.
- (13) Chen, P.; Bai, Y.; Wang, S.; Lyu, M.; Yun, J.-H.; Wang, L. In Situ Growth of 2D Perovskite Capping Layer for Stable and Efficient Perovskite Solar Cells. *Adv. Funct. Mater.* **2018**, 28, 1706923.
- (14) Cho, K. T.; Grancini, G.; Lee, Y.; Oveisi, E.; Ryu, J.; Almora, O.; Tschumi, M.; Schouwink, P. A.; Seo, G.; Heo, S.; Park, J.; Jang, J.; Paek, S.; Garcia-Belmonte, G.; Nazeeruddin, M. K. Selective Growth of Layered Perovskites for Stable and Efficient Photovoltaics. *Energy Environ. Sci.* **2018**, *11*, 952–959.
- (15) Wei, M.; Xiao, K.; Walters, G.; Lin, R.; Zhao, Y.; Saidaminov, M. I.; Todorović, P.; Johnston, A.; Huang, Z.; Chen, H.; Li, A.; Zhu, J.; Yang, Z.; Wang, Y.-K.; Proppe, A. H.; Kelley, S. O.; Hou, Y.; Voznyy, O.; Tan, H.; Sargent, E. H. Combining Efficiency and Stability in Mixed Tin–Lead Perovskite Solar Cells by Capping Grains with an Ultrathin 2D Layer. *Adv. Mater.* 2020, 32, 1907058.
- (16) Zhang, X.; Ren, X.; Liu, B.; Munir, R.; Zhu, X.; Yang, D.; Li, J.; Liu, Y.; Smilgies, D.-M.; Li, R.; Yang, Z.; Niu, T.; Wang, X.; Amassian, A.; Zhao, K.; Liu, S. Stable High Efficiency Two-Dimensional Perovskite Solar Cells via Cesium Doping. *Energy Environ. Sci.* **2017**, 10, 2095–2102.
- (17) Tsai, H.; Nie, W.; Blancon, J.-C.; Stoumpos, C. C.; Asadpour, R.; Harutyunyan, B.; Neukirch, A. J.; Verduzco, R.; Crochet, J. J.; Tretiak, S.; Pedesseau, L.; Even, J.; Alam, M. A.; Gupta, G.; Lou, J.; Ajayan, P. M.; Bedzyk, M. J.; Kanatzidis, M. G.; Mohite, A. D. High-Efficiency Two-Dimensional Ruddlesden—Popper Perovskite Solar Cells. *Nature* **2016**, *536*, 312—316.
- (18) Lee, J.-W.; Dai, Z.; Han, T.-H.; Choi, C.; Chang, S.-Y.; Lee, S.-J.; De Marco, N.; Zhao, H.; Sun, P.; Huang, Y.; Yang, Y. 2D Perovskite Stabilized Phase-Pure Formamidinium Perovskite Solar Cells. *Nat. Commun.* **2018**, *9*, 3021.
- (19) Wang, K.; Wu, C.; Yang, D.; Jiang, Y.; Priya, S. Quasi-Two-Dimensional Halide Perovskite Single Crystal Photodetector. *ACS Nano* **2018**, *12*, 4919–4929.
- (20) Zhu, T.; Yang, Y.; Gu, K.; Liu, C.; Zheng, J.; Gong, X. Novel Quasi-2D Perovskites for Stable and Efficient Perovskite Solar Cells. *ACS Appl. Mater. Interfaces* **2020**, *12*, 51744–51755.

- (21) Li, P.; Zhang, Y.; Liang, C.; Xing, G.; Liu, X.; Li, F.; Liu, X.; Hu, X.; Shao, G.; Song, Y. Phase Pure 2D Perovskite for High-Performance 2D-3D Heterostructured Perovskite Solar Cells. Adv. Mater. 2018, 30, 1805323.
- (22) Liu, Y.; Akin, S.; Pan, L.; Uchida, R.; Arora, N.; Milić, J. V.; Hinderhofer, A.; Schreiber, F.; Uhl, A. R.; Zakeeruddin, S. M.; Hagfeldt, A.; Dar, M. I.; Grätzel, M. Ultrahydrophobic 3D/2D Fluoroarene Bilayer-Based Water-Resistant Perovskite Solar Cells with Efficiencies Exceeding 22%. Sci. Adv. 2019, 5, eaaw2543.
- (23) Wang, F.; Jiang, X.; Chen, H.; Shang, Y.; Liu, H.; Wei, J.; Zhou, W.; He, H.; Liu, W.; Ning, Z. 2D-Quasi-2D-3D Hierarchy Structure for Tin Perovskite Solar Cells with Enhanced Efficiency and Stability. Ioule 2018, 2, 2732-2743.
- (24) Qiu, J.; Xia, Y.; Zheng, Y.; Hui, W.; Gu, H.; Yuan, W.; Yu, H.; Chao, L.; Niu, T.; Yang, Y.; Gao, X.; Chen, Y.; Huang, W. 2D Intermediate Suppression for Efficient Ruddlesden-Popper (RP) Phase Lead-Free Perovskite Solar Cells. ACS Energy Lett. 2019, 4, 1513-1520.
- (25) Wang, K.; Wu, C.; Jiang, Y.; Yang, D.; Wang, K.; Priya, S. Distinct Conducting Layer Edge States in Two-Dimensional (2D) Halide Perovskite. Sci. Adv. 2019, 5, eaau3241.
- (26) Zhang, F.; Kim, D. H.; Lu, H.; Park, J.-S.; Larson, B. W.; Hu, J.; Gao, L.; Xiao, C.; Reid, O. G.; Chen, X.; Zhao, Q.; Ndione, P. F.; Berry, J. J.; You, W.; Walsh, A.; Beard, M. C.; Zhu, K. Enhanced Charge Transport in 2D Perovskites via Fluorination of Organic Cation. J. Am. Chem. Soc. 2019, 141, 5972-5979.
- (27) Ponchai, J.; Kaewurai, P.; Boonthum, C.; Pinsuwan, K.; Supasai, T.; Sahasithiwat, S.; Kanjanaboos, P. Modifying Morphology and Defects of Low-Dimensional, Semi-Transparent Perovskite Thin Films via Solvent Type. RSC Adv. 2019, 9, 12047-12054.
- (28) Yoo, H.-S.; Park, N.-G. Post-Treatment of Perovskite Film with Phenylalkylammonium Iodide for Hysteresis-Less Perovskite Solar Cells. Sol. Energy Mater. Sol. Cells 2018, 179, 57-65.
- (29) Zhang, F.; Huang, Q.; Song, J.; Zhang, Y.; Ding, C.; Liu, F.; Liu, D.; Li, X.; Yasuda, H.; Yoshida, K.; Qu, J.; Hayase, S.; Toyoda, T.; Minemoto, T.; Shen, Q. Growth of Amorphous Passivation Layer Using Phenethylammonium Iodide for High-Performance Inverted Perovskite Solar Cells. Sol. RRL 2020, 4, 1900243.
- (30) Li, N.; Zhu, Z.; Chueh, C.-C.; Liu, H.; Peng, B.; Petrone, A.; Li, X.; Wang, L.; Jen, A. K. Y. Mixed Cation FA_xPEA_{1-x}PbI₃ with Enhanced Phase and Ambient Stability toward High-Performance Perovskite Solar Cells. Adv. Energy Mater. 2017, 7, 1601307.
- (31) Hamill, J. C.; Schwartz, J.; Loo, Y.-L. Influence of Solvent Coordination on Hybrid Organic-Inorganic Perovskite Formation. ACS Energy Lett. 2018, 3, 92-97.
- (32) Guo, X.; McCleese, C.; Gao, W.; Wang, M.; Sang, L.; Burda, C. Investigation of Moisture Stability and PL Characteristics of Terpineol-Passivated Organic-Inorganic Hybrid Perovskite. Mater. Renewable Sustainable Energy 2016, 5, 17.
- (33) Kojima, A.; Teshima, K.; Shirai, Y.; Miyasaka, T. Organometal Halide Perovskites as Visible-Light Sensitizers for Photovoltaic Cells. J. Am. Chem. Soc. 2009, 131, 6050-6051.
- (34) Li, X.; Chen, Y.; Li, L.; Huang, J. Perovskite Thin Film Consisting with One-Dimensional Nanowires. Materials 2018, 11, 1759.
- (35) Zheng, L.; Wang, K.; Zhu, T.; Yang, Y.; Chen, R.; Gu, K.; Liu, C.; Gong, X. High-Performance Perovskite Solar Cells by One-Step Self-Assembled Perovskite-Polymer Thin Films. ACS Appl. Energy Mater. 2020, 3, 5902-5912.
- (36) Wang, K.; Zheng, L.; Zhu, T.; Liu, L.; Becker, M. L.; Gong, X. High Performance Perovskites Solar Cells by Hybrid Perovskites Co-Crystallized with Poly(ethylene oxide). Nano Energy 2020, 67, 104229.
- (37) Xu, W.; Zheng, L.; Zhang, X.; Cao, Y.; Meng, T.; Wu, D.; Liu, L.; Hu, W.; Gong, X. Efficient Perovskite Solar Cells Fabricated by Co Partially Substituted Hybrid Perovskite. Adv. Energy Mater. 2018, 8, 1703178.
- (38) Xu, W.; Zheng, L.; Zhu, T.; Liu, L.; Gong, X. Bulk Heterojunction Perovskite Solar Cells Incorporated with Zn₂SnO₄

- Nanoparticles as the Electron Acceptors. ACS Appl. Mater. Interfaces 2019. 11. 34020-34029.
- (39) Bi, C.; Wang, Q.; Shao, Y.; Yuan, Y.; Xiao, Z.; Huang, J. Non-Wetting Surface-Driven High-Aspect-Ratio Crystalline Grain Growth for Efficient Hybrid Perovskite Solar Cells. Nat. Commun. 2015, 6,
- (40) Seifter, J.; Sun, Y.; Choi, H.; Lee, B. H.; Nguyen, T. L.; Woo, H. Y.; Heeger, A. J. Measurement of the Charge Carrier Mobility Distribution in Bulk Heterojunction Solar Cells. Adv. Mater. 2015, 27, 4989-4996.
- (41) Seifter, J.; Sun, Y.; Heeger, A. J. Transient Photocurrent Response of Small-Molecule Bulk Heterojunction Solar Cells. Adv. Mater. 2014, 26, 2486-2493.
- (42) Cowan, S. R.; Banerji, N.; Leong, W. L.; Heeger, A. J. Charge Formation, Recombination, and Sweep-Out Dynamics in Organic Solar Cells. Adv. Funct. Mater. 2012, 22, 1116-1128.
- (43) Cowan, S. R.; Roy, A.; Heeger, A. J. Recombination in Polymer-Fullerene Bulk Heterojunction Solar Cells. Phys. Rev. B 2010, 82,
- (44) Liu, C.; Wang, K.; Yi, C.; Shi, X.; Smith, A. W.; Gong, X.; Heeger, A. J. Efficient Perovskite Hybrid Photovoltaics via Alcohol-Vapor Annealing Treatment. Adv. Funct. Mater. 2016, 26, 101-110.
- (45) Xu, W.; Zhu, T.; Wu, H.; Liu, L.; Gong, X. Poly(Ethylene Glycol) Diacrylate as the Passivation Layer for High-Performance Perovskite Solar Cells. ACS Appl. Mater. Interfaces 2020, 12, 45045-45055.
- (46) Moiz, S. A.; Khan, I. A.; Younis, W. A.; Karimov, K. S. Space Charge-Limited Current Model for Polymers. Conduct. Polym. 2016,
- (47) Rose, A. Space-Charge-Limited Currents in Solids. Phys. Rev. **1955**, 97, 1538-1544.
- (48) Laban, W. A.; Etgar, L. Depleted Hole Conductor-Free Lead Halide Iodide Heterojunction Solar Cells. Energy Environ. Sci. 2013, 6, 3249-3253.
- (49) Bube, R. H. Trap Density Determination by Space-Charge-Limited Currents. J. Appl. Phys. 1962, 33, 1733-1737.
- (50) Murgatroyd, P. N. Theory of Space-Charge-Limited Current Enhanced by Frenkel Effect. J. Phys. D: Appl. Phys. 1970, 3, 151-156.
- (51) Wei, J.; Guo, F.; Wang, X.; Xu, K.; Lei, M.; Liang, Y.; Zhao, Y.; Xu, D. SnO₂-in-Polymer Matrix for High-Efficiency Perovskite Solar Cells with Improved Reproducibility and Stability. Adv. Mater. 2018, 30, 1805153.
- (52) Gong, X.; Tong, M.; Xia, Y.; Cai, W.; Moon, J. S.; Cao, Y.; Yu, G.; Shieh, C.-L.; Nilsson, B.; Heeger, A. J. High-Detectivity Polymer Photodetectors with Spectral Response from 300 nm to 1450 nm. Science 2009, 325, 1665.
- (53) Dou, L.; Yang, Y.; You, J.; Hong, Z.; Chang, W.-H.; Li, G.; Yang, Y. Solution-Processed Hybrid Perovskite Photodetectors with High Detectivity. Nat. Commun. 2014, 5, 5404.
- (54) Jha, A. R. Infrared Technology, Applications to Electro-Optics, Photonic Devices, and Sensors. Infrared 2000, 11, 1944-1948.
- (55) Sze, S. M.; Ng, K. K.; Physics of Semiconductor Devices; John wiley & sons, 2006.
- (56) Gao, L.; Zeng, K.; Guo, J.; Ge, C.; Du, J.; Zhao, Y.; Chen, C.; Deng, H.; He, Y.; Song, H.; Niu, G.; Tang, J. Passivated Single-Crystalline CH3NH3PbI3 Nanowire Photodetector with High Detectivity and Polarization Sensitivity. Nano Lett. 2016, 16, 7446-7454.
- (57) Fang, Y.; Huang, J. Resolving Weak Light of Sub-picowatt per Square Centimeter by Hybrid Perovskite Photodetectors Enabled by Noise Reduction. Adv. Mater. 2015, 27, 2804-2810.
- (58) Xia, H.; Tong, S.; Zhang, C.; Wang, C.; Sun, J.; He, J.; Zhang, J.; Gao, Y.; Yang, J. Flexible and Air-Stable Perovskite Network Photodetectors Based on CH₃NH₃PbI₃/C8BTBT Bulk Heterojunction. Appl. Phys. Lett. 2018, 112, 233301.
- (59) Fang, Y.; Dong, Q.; Shao, Y.; Yuan, Y.; Huang, J. Highly Narrowband Perovskite Single-Crystal Photodetectors Enabled by Surface-Charge Recombination. Nat. Photonics 2015, 9, 679-686.

- (60) Shen, L.; Fang, Y.; Wang, D.; Bai, Y.; Deng, Y.; Wang, M.; Lu, Y.; Huang, J. A Self-Powered, Sub-nanosecond-Response Solution-Processed Hybrid Perovskite Photodetector for Time-Resolved Photoluminescence-Lifetime Detection. *Adv. Mater.* **2016**, 28, 10794—10800.
- (61) Hegedus, S. S.; Shafarman, W. N. Thin-Film Solar Cells: Device Measurements and Analysis. *Prog. Photovoltaics* **2004**, *12*, 155–176.
- (62) Xu, W.; Guo, Y.; Zhang, X.; Zheng, L.; Zhu, T.; Zhao, D.; Hu, W.; Gong, X. Room-Temperature-Operated Ultrasensitive Broadband Photodetectors by Perovskite Incorporated with Conjugated Polymer and Single-Wall Carbon Nanotubes. *Adv. Funct. Mater.* **2018**, 28, 1705541.